Journal of Alloys and Compounds 821 (2020) 153518

Contents lists available at ScienceDirect

Journal of Alloys and Compounds

journal homepage: http://www.elsevier.com/locate/jalcom

Review

Effect of Ti addition on microstructure evolution and precipitation in Cu–Co–Si alloy during hot deformation

Yongfeng Geng [a, b, c, 1], Xu Li [d, 1], Honglei Zhou [g, 1], Yi Zhang [a, b, c, *], Yanlin Jia [e, **], Baohong Tian [a, b, c], Yong Liu [a, b, c], Alex A. Volinsky [f], Xiaohui Zhang [a, b, c], Kexing Song [a, b, c], Guangxin Wang [a, b, c], Lihua Li [a, b, c], Jinrui Hou [a, b, c]

[a] School of Materials Science and Engineering, Henan University of Science and Technology, Luoyang, 471023, PR China
[b] Provincial and Ministerial Co-construction of Collaborative Innovation Center for Non-ferrous Metal New Materials and Advanced Processing Technology, Henan Province, Luoyang, 471023, PR China
[c] Henan Province Key Laboratory of Nonferrous Materials Science and Processing Technology, Luoyang, 471023, PR China
[d] Center for Advanced Measurement Science, National Institute of Metrology, Beijing, 100029, PR China
[e] College of Materials Science and Engineering, Beijing University of Technology, Beijing, 100124, PR China
[f] Department of Mechanical Engineering, University of South Florida, Tampa, 33620, USA
[g] School of Materials Science and Engineering, Shanghai University of Technology, Shanghai, 200000, PR China

ARTICLE INFO

Article history:
Received 8 October 2019
Received in revised form
14 December 2019
Accepted 23 December 2019
Available online 24 December 2019

Keywords:
Cu-Co-Si and Cu–Co–Si–Ti alloys
Hot compression
Flow stress
Microstructure evolution
Texture

ABSTRACT

Hot compression behavior of the Cu–Co–Si and Cu–Co–Si–Ti alloys was studied using the Gleeble-1500 simulator at 0.001–10 s^{-1} strain rate and 500–900 °C deformation temperature. Ti addition increased the flow stress of the Cu–Co–Si–Ti alloy compared with the Cu–Co–Si alloy at the same deformation conditions. With the deformation temperature increased from 700 °C to 900 °C, the Cu–Co–Si alloy texture transformed from the copper texture to the R texture. Due to the addition of Ti, the copper texture and R texture were substituted by the Goss texture and the copper texture, respectively. The constitutive models of the Cu–Co–Si and Cu–Co–Si–Ti alloys hot deformation behavior were obtained. The activation energy of the Cu–Co–Si alloy was 411.648 kJ/mol, and the activation energy of the Cu–Co–Si–Ti alloy was 500.794 kJ/mol, which is 27% higher. The precipitated Co_2Si phase was found in both Cu–Co–Si and Cu–Co–Si–Ti alloys deformed at 700 °C and 0.001 s^{-1}. In addition, the CoSi and Cu_4Ti phases were found in the Cu–Co–Si and Cu–Co–Si–Ti alloys, respectively. The strengthening mechanisms, including dispersion strengthening, twinning and grain refinement strengthening, control the Cu–Co–Si–Ti alloy hot deformation, and lead to increased flow stress and activation energy, and inhibit dynamic recrystallization of the Cu–Co–Si–Ti alloy.

© 2019 Elsevier B.V. All rights reserved.

Contents

* Corresponding author. School of Materials Science and Engineering, Henan University of Science and Technology, Luoyang, 471023, PR China.
** Corresponding author. College of Materials Science and Engineering, Beijing University of Technology, Beijing, 100124, PR China.
E-mail addresses: zhshgu436@163.com (Y. Zhang), jiayanlin@126.com (Y. Jia).
[1] These authors contributed equally to this work.

https://doi.org/10.1016/j.jallcom.2019.153518
0925-8388/© 2019 Elsevier B.V. All rights reserved.

1. Introduction

Copper and copper alloys are widely used in different applications due to their excellent electrical conductivity and mechanical properties [1,2]. For example, they can be used in electronics, contact wires, lead frame, etc. [3–5]. In recent years, with the development of lead frame and contact wires, the performance requirements for copper alloys have increased rapidly [6]. The common strengthening method for copper alloys is adding alloying elements, such as Be [7], Ag [8], Co [9], Ti [10], and so on. While the addition of alloying elements slightly decreased the electrical conductivity, the hot working and mechanical properties were greatly improved. Chihiro et al. [11] analyzed the structure and aging behaviors of the Cu–Be alloy. It was found that the ultra-high hardness and ultra-fine grains of Cu–Be alloy were obtained after aging treatment. Despite the obtained excellent properties, the Cu–Be alloy has been replaced by other alloys, such as Cu–Ni–Si, Cu–Cr–Zr, and Cu–Ag, due to the environmental hazards of Be [12].

Zhao et al. [13] investigated the effects of Co addition on the microstructure and physical properties of Cu–Ni–Si alloys and observed that the Co_2Si precipitation phase can improve the conductivity and mechanical properties of the alloy during aging. Zhou et al. [14] proved that the phase transition sequence during aging was γ''- γ' -γ for the Cu-0.23Be-0.84Co alloy. In addition, the conductivity and hardness of the alloy obtained peak values due to the occurrence of the γ′ phase, which was coherent with the matrix. Krishna et al. [15] found that the Co_2Si precipitate during aging can improve the conductivity and strength of the Cu–Ni–Si–Co–Zr alloy. It can be found that the Co_2Si precipitate can be formed due to the strong bonding between Co and Si during the aging process, which can significantly improve the mechanical properties of copper. Although the addition of Co reduces the conductivity of the alloy, it can greatly improve the strength, toughness and hot working properties of copper. The addition of Si can improve the mechanical properties, pressure processing properties and corrosion resistance of copper. Thus, a better performance alloy can be obtained by adding Co and Si into pure copper based on the above investigations.

Kim et al. [16] demonstrated that the addition of Ti improved the conductivity and mechanical properties of the alloy by promoting precipitation of fine δ-Ni_2Si and Ni–Si–Ti phases. Liu et al. [17] analyzed the conductivity and mechanical properties of the Cu–3Ti–3Ni alloy during aging and proved that the conductivity and hardness increased due to the Ni_3Ti precipitation and coherent Cu_4Ti. It is well known that Ti and Cu have relatively strong bonding and form Cu_4Ti, which can improve the conductivity and mechanical properties of copper. The addition of Ti can improve the strength, impact toughness and hot working properties of copper.

Based on the above experiments, Cu–Co–Si alloy was obtained by adding Co and Si in a certain proportion to copper. The multiphase strengthened Cu–Co–Si alloy with Ti addition was also obtained. There are several investigations of the aging behaviors of Cu–Co–Si alloys. However, the hot deformation behavior of Cu–Co–Si alloys has been rarely investigated. Moreover, there are no detailed investigations of the effects of Ti addition on the microstructure evolution and the flow stress during hot deformation tests. Thus, the effects of Ti addition on the hot compression behavior of the Cu–Co–Si alloy by hot compression test were investigated in this paper. The hot compression tests were carried out using the Gleeble-1500 simulator at 0.001–10 s^{-1} strain rate and 500–900 °C deformation temperature. The effects of Ti addition on the flow stress, microstructure evolution, electron backscatter diffraction (EBSD) images, and activation energy were compared. The precipitates of the Cu–Co–Si and Cu–Co–Si–Ti alloy were also analyzed.

2. Materials and experimental procedures

The Cu–1Co-0.65Si and Cu–1Co-0.65Si-0.1Ti (wt.%) alloys were obtained by vacuum melting of pure Si, pure Co, standard cathode copper with 99.9% mass fraction and Cu-45% Ti master alloy. The ZG-0.01-40-4 vacuum medium frequency induction furnace was used for vacuum smelting. In addition, the argon was needed in the process of melting as a protective atmosphere to prevent material oxidation during vacuum smelting. The temperature of the furnace was kept at 1150–1250 °C, and the alloy was poured into the crucible with the internal diameter of ~90 mm, ~20 mm thickness and ~190 mm height. The nominal and analyzed composition for two alloys is listed in Table 1. After cooling to the room temperature, the ingots were homogenized at 960 °C for 1 h and then extruded into 20 mm diameter bars by the XJ-500 metal profile extrusion machine. In addition, the bars were treated by solid solution treatment at 960 °C for 1 h and cut intoϕ8 mm × 12 mm cylinders by wire cutting before the hot compression tests using the Gleeble-1500D thermo-mechanical simulator. According to the Cu–Co phase diagram shown in Fig. 1(a), the room temperature phases are Cu and ε -Co. The hot compression tests were carried out at 500–900 °C temperature and 0.001–10 s^{-1} strain rates range. As shown in Fig. 1(b), the specimens were heated to the experimental temperature at 10 °C/s and then compressed to 55% total deformation after holding for 3 min. Finally, water quenching was used to retain the high-temperature structure. Fig. 1(d) shows the hot compression loading. The hole with 0.5 mm diameter was used to insert thermocouples.

In order to analyze the microstructure evolution of the Cu–Co–Si and Cu–Co–Si–Ti alloys during hot deformation, the specimens were cut along the longitudinal plane in Fig. 1(c). The central parts of the samples were polished, etched, and then

Table 1
The nominal and analyzed composition of the alloys.

Nominal composition (wt. %)	Analyzed composition (wt. %)			
	Co	Si	Ti	Cu
Cu–1Co-0.65Si	0.952	0.641	–	Bal.
Cu–1Co-0.65Si-0.1Ti	0.895	0.601	0.094	Bal.

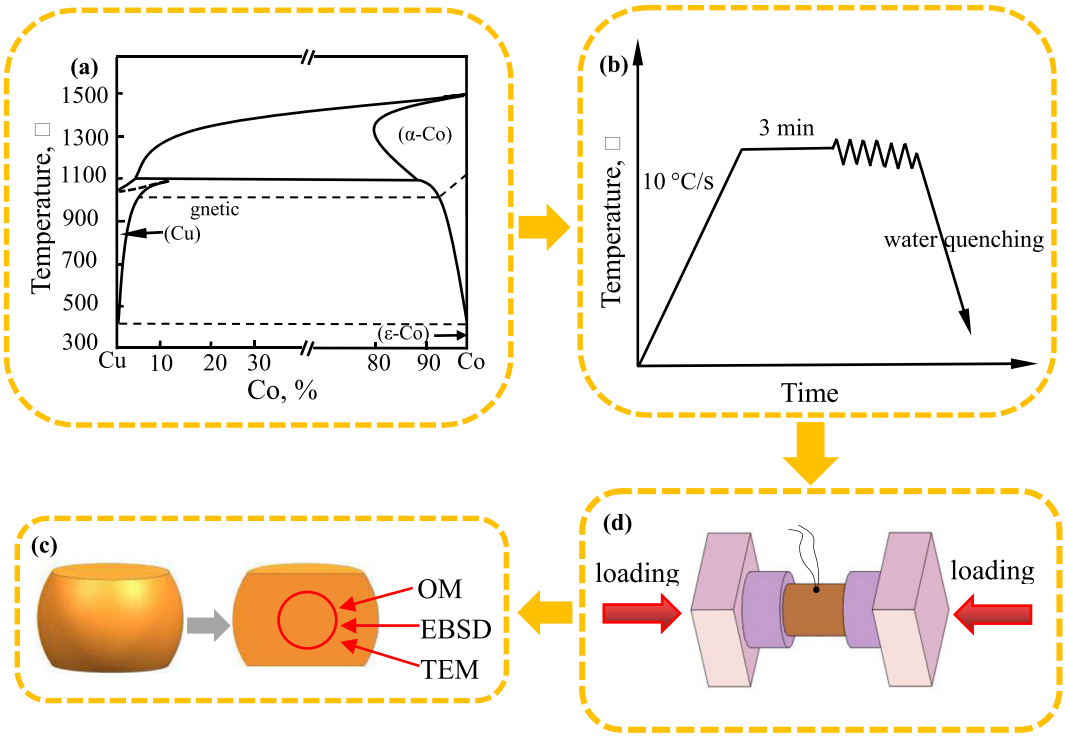

Fig. 1. Schematic representation of (a) Cu–Co phase diagram [18,19]; (b) hot compression process; (c) the testing positions of OM, EBSD and TEM; (d) hot compression loading.

observed by the Olympus PMG3 optical microscope (OM). The etching solution used was 3.5 g $FeCl_3$, 5 ml HCl and 95 ml anhydrous alcohol. In addition, the samples were electro-polished with a magnetic stirrer and then used for EBSD (electron backscatter diffraction) observations. And the polishing solution is made of phosphoric acid and alcohol in a ratio of 1:1, which is the key step in the preparation of EBSD samples. The EBSD images were obtained using the JSM-7800F backscatter scanning electron microscope (SEM). The samples with 3 mm diameter and 100 μm thickness were ion thinned by the Gatan 691 ion thinner. After that, the samples were observed by transmission electron microscopy using the JEM-2100 transmission electron microscope (TEM).

3. Results

3.1. Flow stress

The thermal deformation process of materials consists of work hardening, dynamic recovery and dynamic recrystallization [20–22]. In the early stage of deformation, the flow stress increases sharply, representing work hardening. The dislocation density increases during the thermal deformation of the material and finally leads to dislocation entanglement at deformation zones and work hardening. Otherwise, the high lattice distortion energy can provide a driving force for dynamic recovery and dynamic recrystallization. This is the reason why the flow stress tends to flatten or decrease. Thus, the flow stress increases with the decrease in temperature or the increase of the strain rate. In addition, the values of the flow stress are affected by the strain rate and deformation temperature [23,24].

Fig. 2 shows the true stress-true strain curves of the Cu–Co–Si and Cu–Co–Si–Ti alloys deformed at 0.01 s^{-1}, 0.1 s^{-1}, 800 °C and 900 °C, respectively. The flow stress increases rapidly at the early stage of hot deformation, representing the work hardening characteristics. The flow stress curves tend to be flat or decrease at higher deformation temperature or lower strain rate due to the dynamic recovery and dynamic recrystallization. Fig. 2(a) and (b) illustrate the flow stress of the two alloys deformed at 0.01 s^{-1} and 0.1 s^{-1}, respectively. The peak flow stress values of Cu–Co–Si were 233 MPa and 210 MPa, deformed at the strain rate of 0.1 s^{-1} with different temperature of 500 °C and 600 °C temperature, respectively. The flow stress decreases with the increase of temperature. However, the peak values of Cu–Co–Si–Ti alloy were 258 MPa and 219 MPa at the same conditions. Fig. 2(c) and (d) show the flow stress of the two alloys deformed at 800 °C and 900 °C, respectively. Similar to Fig. 2(a) and (b), dynamic recrystallization occurs at a lower strain rate. In addition, the flow stress increases with the increase of strain rate. For instance, the peak stress values of the Cu–Co–Si alloy are 56 MPa and 70 MPa, respectively, which were deformed at 800 °C with different strain rates of 0.01 s^{-1} and 0.1 s^{-1}. Consequently, the flow stress decreases with the increased temperature or the decreased strain rate, which can be explained by easier dynamic recrystallization at higher temperature or lower strain rate.

Compared to the true stress-true strain curves in Fig. 2, the addition of Ti increases the flow stress of the alloy. The addition of Ti promotes the precipitation, and the precipitated particles pin at the grain boundaries and dislocations, which hinders the movement of dislocations and grain boundaries. Eventually, the flow stress of the Cu–Co–Si–Ti alloy increases. This was also verified by some researchers' results. For example, Qiu et al. [25] confirmed that the addition of 0.008% Ti can promote the precipitation of nano-sized carbides. The Y/Y–Ti inclusions pinned the austenite grain boundaries. Zhou et al. [26] reported that the addition of Ti produced fine Y–Ti–O complex oxides, which can improve the tensile strength of 9Cr ODS steels.

3.2. Microstructure evolution

Fig. 3(a) and (b) show the microstructure of the Cu–Co–Si and

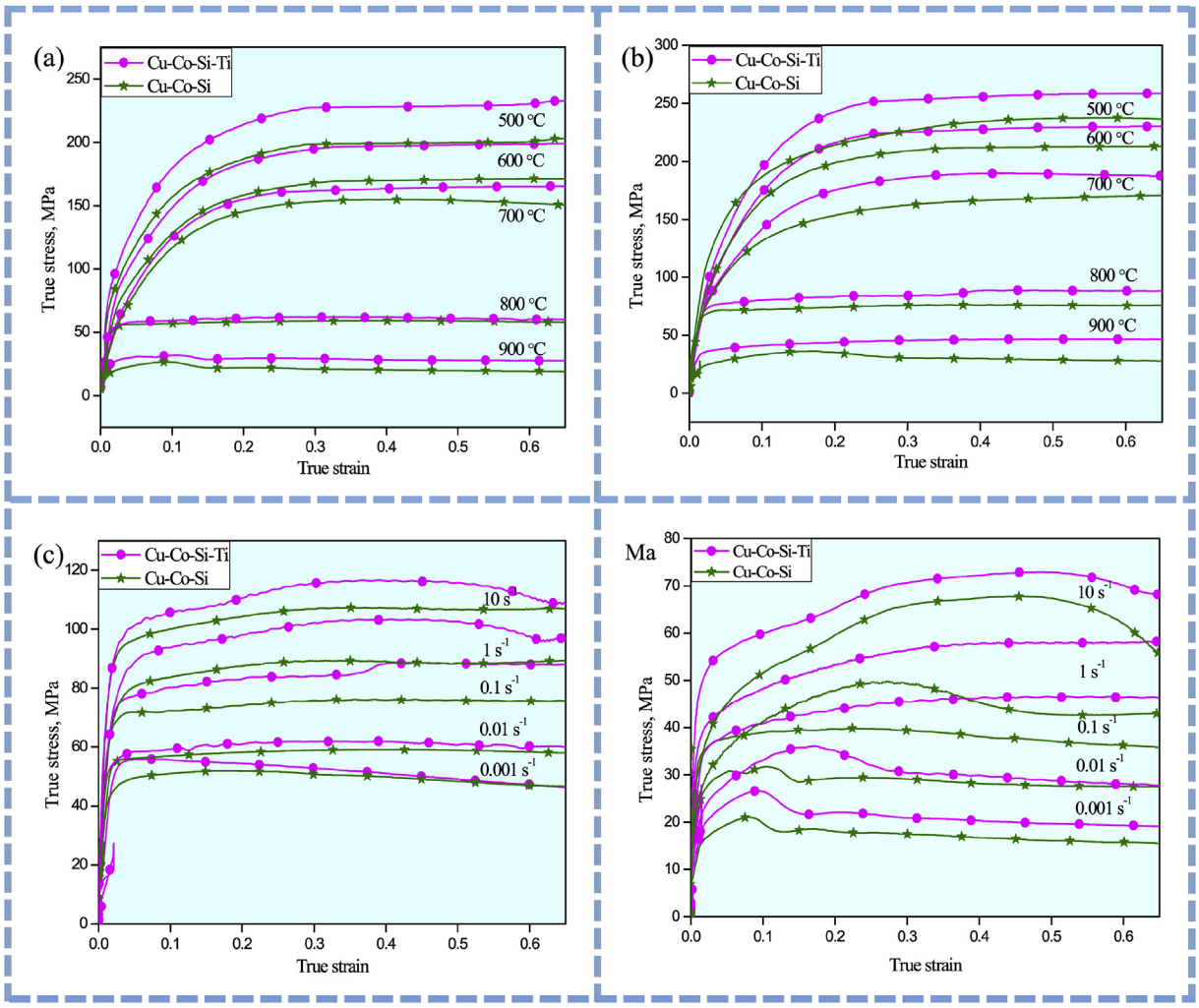

Fig. 2. The true s tress-true strain of Cu–Co–Si and Cu–Co–Si–Ti alloys deformed at (a) 0.01 s^{-1}, (b) 0.1 s^{-1}, (c) 800 °C, (d) 900 °C.

Cu–Co–Si–Ti alloys extruded at 960 °C, respectively. The structure of the two alloys after solution treatment at 960 °C for 1 h is shown in Fig. 3(c) and (d), respectively. The grain size of the two alloys increased after the solid solution treatment.

According to Fig. 2, dynamic recrystallization occurs easier at higher deformation temperature or lower strain rate. Microstructure evolution observation is a direct method for studying the process of dynamic recrystallization. The microstructure evolution of the Cu–Co–Si and Cu–Co–Si–Ti alloys deformed at 0.001 s^{-1} and 700–900 °C was observed. Fig. 4 and Fig. 5 show the microstructure of the Cu–Co–Si and Cu–Co–Si–Ti alloys deformed at 0.001 s^{-1} and 700–900 °C, respectively. In Fig. 4(a) partial recrystallization grains exist in the fiber structure. Fig. 4(b) is a magnification of the red area in Fig. 4(a). There are a large number of dynamically recrystallized grains (DRX [27]) at grain boundaries in the yellow rectangle, which represents dynamic recrystallization. The reason is that dislocations tangles are caused by inhibiting the movement of dislocations, leading to a large amount of stored energy at grain boundaries. The dislocation energy stored at grain boundaries can provide the driving force for dynamic recrystallization. Thus, the dynamic recrystallization grains nucleate preferentially at grain boundaries. Dynamic recrystallization grains growth with deformation temperature was further increased in Fig. 4(c) and (d). Fig. 4(d) shows that the grains completely grew when deformed at 900 °C, representing the completion of dynamic recrystallization. The similar phenomenon can be also observed in the deformation process of the Cu–Co–Si–Ti alloy in Fig. 5(a–d). The difference is that the process of dynamic recrystallization was slower compared with the Cu–Co–Si alloy due to the addition of Ti when deformed at 0.001 s^{-1} and 700–800 °C. The effects of Ti addition on the structure were not obvious with further temperature increase to 900 °C because dynamic recrystallization is more efficient at higher deformation temperature.

EBSD can be used to analyze the microstructure and orientation of solid crystal materials under various processing conditions. In addition, the textures of face-centered cubic metals include the {011} <100> Goss texture, {112} <111> copper texture, {111} <211> R texture, {001} <100> cubic texture and {011} <211> brass texture [28]. In order to investigate the texture and misorientation angle of the Cu–Co–Si and Cu–Co–Si–Ti alloys during hot deformation, the samples were observed by the JSM-7800F backscatter scanning electron microscope.

Fig. 6 shows the orientation maps and {100}, {110}, and {111} pole figures of the two alloys deformed at 0.001 s^{-1} and different temperatures of 700 °C and 900 °C, respectively. As shown in Fig. 6(a_1-d_1), there are three main colors in the orientation maps, which are mainly caused by the different orientation of grains. Corresponding to Fig. 4(a) and (d), in Fig. 6(a_1) and (b_1), there are

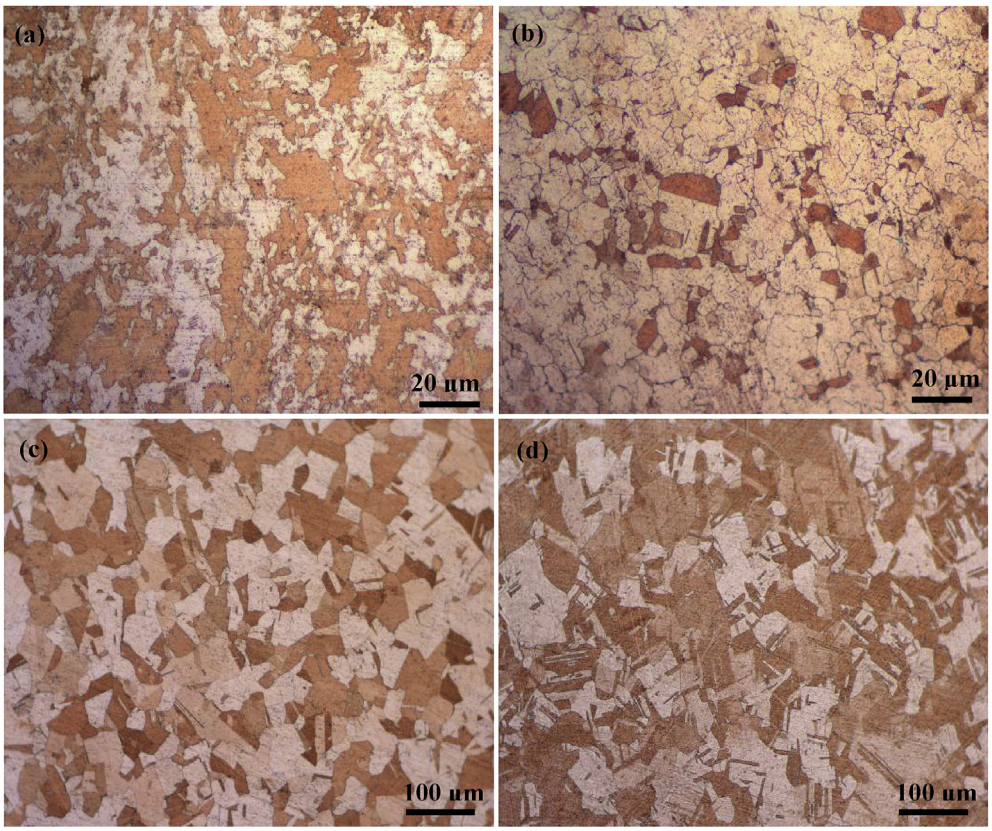

Fig. 3. Structure of specimens: extruded at 960 °C (a) Cu–Co–Si alloy, (b) Cu–Co–Si–Ti alloy; as solid solution state(c) Cu–Co–Si alloy,(d) Cu–Co–Si–Ti alloy.

numerous dynamic recrystallization grains deformed at 700 °C and 0.001 s^{-1}. Increasing the temperature to 900 °C caused grain growth. Fig. 6(a_2) shows {100}, {110}, and {111} pole figures, and the {112} <111> copper texture was confirmed by referring to the standard polar figures. With the deformation temperature increase, the {111} <211> R texture appeared in Fig. 6(b_2) due to further dynamic recrystallization. In addition, the EBSD images in Fig. 6(c_1) and (d_1) are consistent with Fig. 5(a) and (d), which have similar phenomena with Fig. 6(a_1) and (b_1). However, the difference is that the texture of the Cu–Co–Si–Ti alloy in Fig. 6(c_2) and (d_2) was strengthened compared with Fig. 6(a_2) and (b_2). In other words, the {112} <111> copper texture and {111} <211> R texture were substituted by the {011} <100> Goss texture and the {112} <111> copper texture, respectively. Generally, recrystallized particle-induced nucleation energy and stacking fault energy [29] are the main factors affecting the texture of materials. {112} <111> copper texture usually appears in face-centered cubic metals with intermediate and high stacking fault energy.

Fig. 7 shows the distribution of misorientation angles at different deformation conditions of the two alloys, which are related to dislocation density [30]. The misorientation angles of the Cu–Co–Si and Cu–Co–Si–Ti alloys deformed at 0.001 s^{-1} and different temperatures are mainly low angles. The percent of the low misorientation angles distribution in the Cu–Co–Si–Ti alloy is higher than in the Cu–Co–Si alloy under the same deformation conditions. The misorientation angles distribution decreases with temperature increasing from 700 °C to 900 °C for the same alloy. The dislocation density at 700 °C is higher than at 900 °C for the same alloy, which corresponds to the structural evolution in Figs. 4 and 5. Dynamic recrystallization proceeded and dislocation density decreased with temperature. Other misorientation angles have similar trends as the low angles in Fig. 7(a) and (b).

It is well known that the migration rate of grain boundaries is related to the dislocation density near the grain boundary. And the geometrically necessary dislocation (GND) density is related to the Kernel Average Misorientation (KAM) as follows [31]:

$$\rho^{GND} = \frac{2\theta}{\mu b} \tag{1}$$

where ρ^{GND} is the geometrically necessary dislocation (GND) density (m^{-2}), θ is the average local misorientation (rad), μ is the step size of the experiment (5 μm), and b is the Burger's vector (2.55 nm) which can be calculated by $b = \frac{a}{2}<110>$. It is defined that the critical value of the average local misorientation as 3°. Any misorientation larger than this value is excluded in the local misorientation calculation since it is caused by the grain boundary, not by the GND accumulation.

Fig. 8 shows the Kernel Average Misorientation (KAM) of the two alloys deformed at 0.001 s^{-1} and different temperatures of 700 °C and 900 °C, respectively. And the geometrically necessary dislocation (GND) density is 4.3×10^{13} m^{-2}, 3.4×10^{13} m^{-2}, 4.8×10^{13} m^{-2} and 3.9×10^{13} m^{-2}, respectively in Fig. 8(a–d). It can be seen that the addition of Ti increases the geometrically necessary dislocation (GND) density of the alloy, and the increase of temperature decreases the geometrically necessary dislocation (GND) density, which indicates that the dislocation density rises with the decrease of temperature or the increase of strain rate. The effect of the Ti addition on the dislocation density is similar to that on flow stress as displayed in Fig. 2.

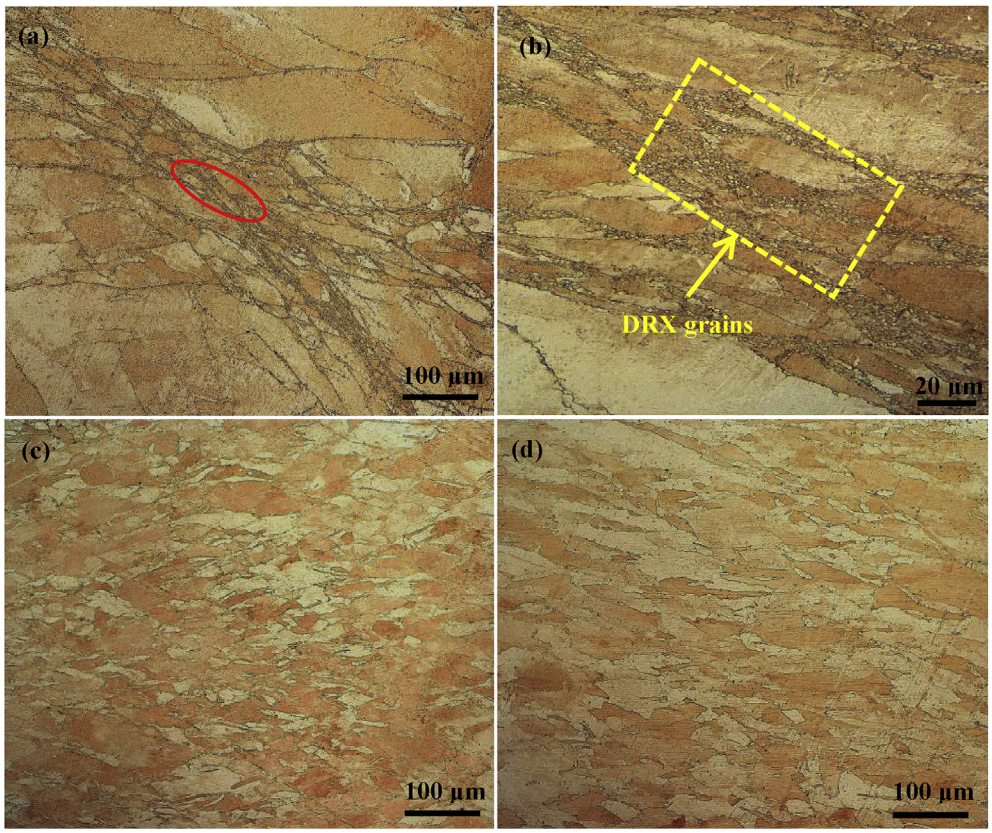

Fig. 4. Structure of Cu–Co–Si alloy deformed at 0.001 s^{-1} and different temperatures (a) 700 °C; (b) magnification of red circle in (a); (c) 800 °C; (d) 900 °C. (For interpretation of the references to color in this figure legend, the reader is referred to the Web version of this article.)

3.3. Constitutive equation

Activation energy is the energy "threshold" that metal atoms need to cross when plastic deformation occurs and is important for evaluating metals hot workability. The constitutive equation can be used to describe the relationships between the flow stress, thermal deformation temperature, and strain rate. Based on the experimental data of hot deformation, the activation energy is calculated, and the constitutive equations are established for the two alloys in this section.

According to the model proposed by Sellars and McTegart [32], the relationship between the peak stress, strain rate, and deformation temperature can be obtained as follows:

$$\dot{\varepsilon} = A\left[sinh(\alpha\sigma)^{n} exp\left(-\frac{Q}{RT}\right)\right] \tag{2}$$

Eq. (2) can be expressed by using the following equations according to the strain magnitude:

$$\dot{\varepsilon} = A_1\sigma^{n_1} exp\left[-\frac{Q}{RT}\right] \quad (\alpha\sigma < 0.8) \tag{3}$$

$$\dot{\varepsilon} = A_2 exp(\beta\sigma) exp\left[-\frac{Q}{RT}\right] \quad (\alpha\sigma > 1.2) \tag{4}$$

Here, $\dot{\varepsilon}$ is the strain rate, σ is the peak stress, Q is the activation energy, A, A_1, A_2,α, β, n_1, n, and R are constants, and T is the deformation temperature in K.

Taking the natural logarithms of Eqs. (2)–(4), respectively, gives:

$$\ln\dot{\varepsilon} = n\ln[\sinh(\alpha\sigma)] - \frac{Q}{RT} + \ln A \tag{5}$$

$$\ln\dot{\varepsilon} = n_1\ln\sigma + \ln A_1 - \frac{Q}{RT} \tag{6}$$

$$\ln\dot{\varepsilon} = \beta\sigma + \ln A_2 - \frac{Q}{RT} \tag{7}$$

Taking partial derivatives of Eq. (2) yields:

$$Q = R\left[\frac{\partial(\ln\dot{\varepsilon})}{\partial\ln[\sin\alpha\sigma]}\right]_T\left[\frac{\partial\ln[\sinh\alpha\sigma]}{\partial\left(1/T\right)}\right] = RnS \tag{8}$$

Lattice self-diffusion energy due to the dislocation slip and climb can be expressed in the Zenner parameter, Z [33,34]:

$$Z = \dot{\varepsilon} exp\left[\frac{Q}{RT}\right] \tag{9}$$

Using it in Eq. (2) and taking natural logarithms of both sides gives:

$$\ln Z = \ln A + n[\ln\sinh(\alpha\sigma)] \tag{10}$$

The Cu–Co–Si alloy was used as an example to calculate the activation energy. Fig. 9 shows the relationship between the peak stress, strain rate and deformation temperature of the Cu–Co–Si alloy. Fig. 9(a–d) show the relationships between ln (strain rate)

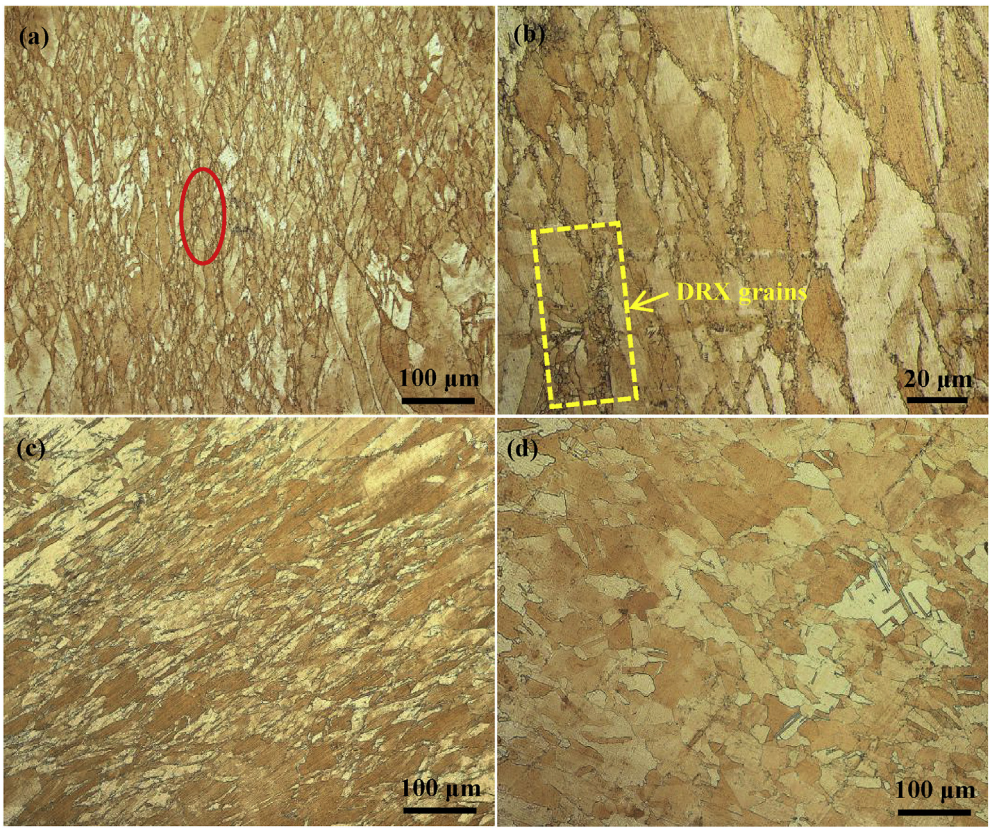

Fig. 5. Structure of Cu–Co–Si–Ti alloy deformed at 0.001 s^{-1} and different temperatures (a) 700 °C; (b) magnification of red circle in (a); (c) 800 °C; (d) 900 °C. (For interpretation of the references to color in this figure legend, the reader is referred to the Web version of this article.)

and lnσ, ln (strain rate) and σ, ln (strain rate) and ln [sinh (ασ)], and ln [sinh (ασ)] and $T^{-1} * 10^3$ K^{-1}, respectively. Here, n_1, β, n, and S are the average slopes of (a-d). Thus, the values of n_1, β are 15.333, 0.172, and then $\alpha = \beta/n_1 = 0.011$, $n = 10.773$, $S = 4.596$. Finally, $Q = RnS = 411.648$ kJ/mol. The corresponding activation energy of the Cu–Co–Si–Ti alloy is 500.794 kJ/mol. The intercept of Cu–Co–Si alloy is 47.41, calculated according to Fig. 9(d), and the corresponding intercept for the Cu–Co–Si–Ti alloy is 57.372. Thus, the constitutive equations of the Cu–Co–Si and Cu–Co–Si–Ti alloys are:

For the Cu–Co–Si alloy:

$$\dot{\varepsilon} = e^{47.410}[\sinh(0.011\sigma)]^{10.773} exp\left(-\frac{411648}{8.314T}\right)$$

For the Cu–Co–Si–Ti alloy:

$$\dot{\varepsilon} = e^{57.372}[\sinh(0.009\sigma)]^{12.89} exp\left(-\frac{500794}{8.314T}\right)$$

Fig. 9(f) shows the activation energy of pure copper, Cu–Co–Si and Cu–Co–Si–Ti alloys. The activation energy of the Cu–Co–Si and Cu–Co–Si–Ti alloys is much higher than pure copper. The activation energy of the Cu–Co–Si alloy increased by 27% due to the addition of Ti.

Shukla et al. [35] confirmed that the activation energy of the Cu–Cr–Nb alloy is expected to be higher due to the presence of Cr_2Nb precipitates, which can interact with dislocations, nail dislocations and hinder their movement. Wang et al. [36] observed that Ce addition increased the activation energy of Cu–Mg alloy. The reason is that the addition of Ce promotes the precipitation of phases, such as CeO_2, which nails dislocations and grain boundaries, and prohibits the movement of dislocations. Finally, the activation energy increased. The reason may be that the addition of Ti promotes precipitation, which can prohibit the movement of dislocations. The specific reasons are discussed below.

4. Discussion

4.1. Effects of Ti addition on precipitates

Many researchers have shown that the addition of rare earth alloying elements can promote secondary phases precipitation. For instance, Zhao et al. [37] investigated the conductivity and mechanical properties of the Cu–Ni–Si–Co–Cr alloy during aging. It has been proven that the addition of Co can promote precipitation of Cr, Ni and Si, forming $(Cr, Co)_2Si$, $(Ni, Co)_2Si$ and Cr precipitates. Xiao et al. [38] demonstrated that δ-Ni_2Si and $(Ni, Co)_2Si$ were formed during aging at 400–600 °C. Liu et al. [39] investigated the hot deformation behavior of the Cu–3Ti–3Ni-0.5Si alloy, and the Ni_2Si and Ni_3Ti phases were determined by TEM.

In order to clarify the effects of Ti addition on precipitates during hot deformation of the Cu–Co–Si and Cu–Co–Si–Ti alloys, the structure of the two alloys deformed at 700 °C and 0.001 s^{-1} was analyzed by TEM, shown in Fig. 10 and Fig. 11. Fig. 10(a and b) shows the bright field and dark field images of Cu–Co–Si alloy deformed at 700 °C and 0.001 s^{-1}, respectively. The precipitates are mainly distributed in the grain interior. Entangled dislocations were formed during thermal deformation due to the existence of precipitates and grain boundaries, which hindered the dislocation movement. Furthermore, Fig. 10(c) is the magnification of the red rectangular area in Fig. 10(b), and the average precipitate size is about 40 nm. Fig. 10(d) is the small area diffraction pattern (SADP)

of the precipitate in Fig. 10(c). It can be determined that the precipitate is Co_2Si, which has an orthorhombic structure, and the lattice parameters are a = 7.109 nm, b = 4.918 nm, c = 3.737 nm, and $\alpha = \beta = \gamma = 90°$. Fig. 10(e) shows the TEM image of another precipitate with the 28 nm size, and it can be determined from Fig. 10(f) that the precipitate is CoSi, which has a cubic structure and the lattice parameters are a = b = c = 4.4463 and $\alpha = \beta = \gamma = 90°$.

Fig. 11 shows the TEM image of the Cu–Co–Si–Ti alloy

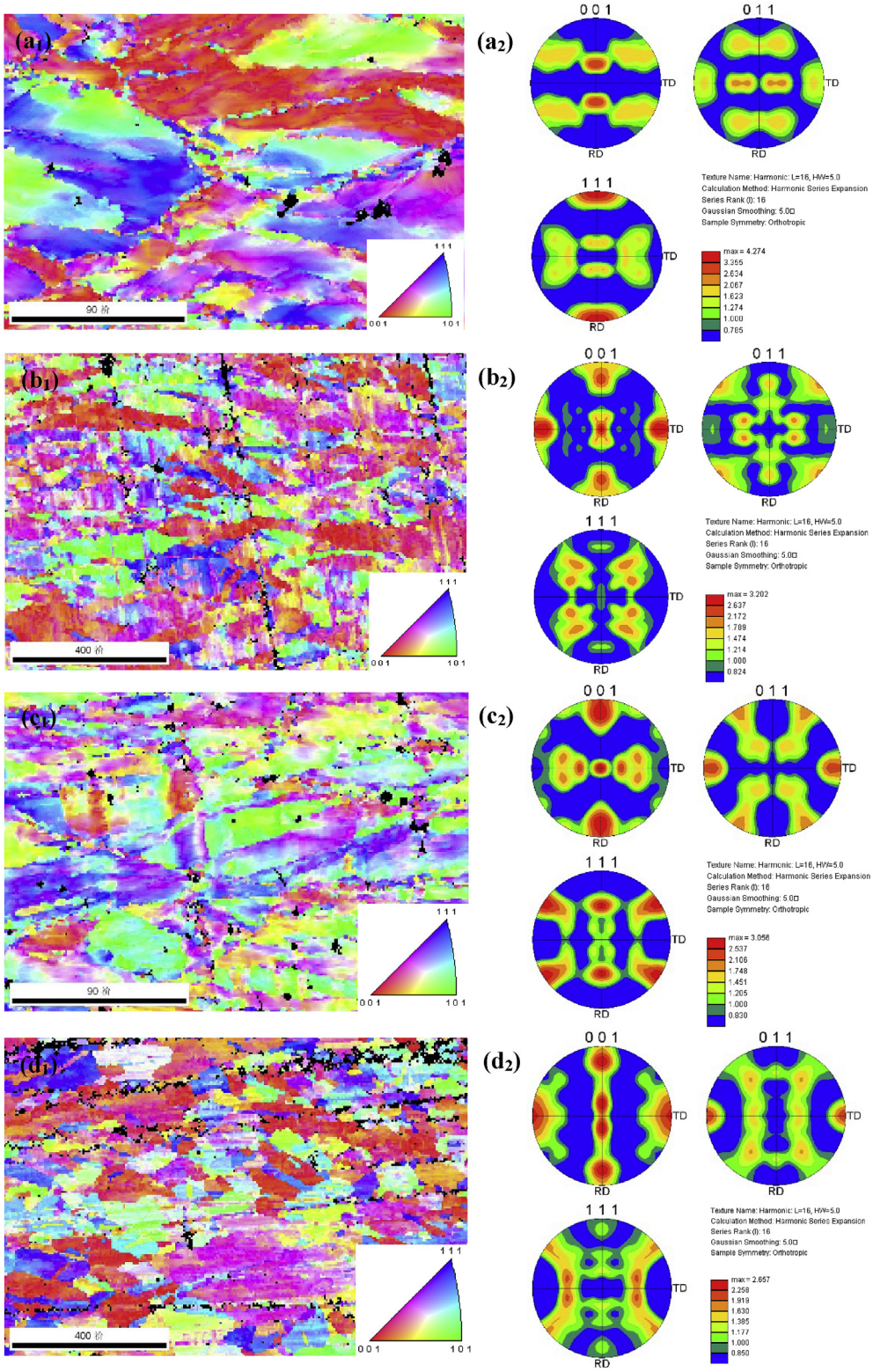

Fig. 6. EBSD orientation maps and {100},{110}, {111}pole fgures of (a)Cu–Co–Si alloy deformed 700 °C,0.001 s^{-1};(b)Cu–Co–Si alloy deformed 900 °C,0.001 s^{-1};(c)Cu–Co–Si–Ti alloy deformed 700 °C,0.001 s^{-1};(d)Cu–Co–Si–Ti alloy deformed 900 °C,0.001 s^{-1}.

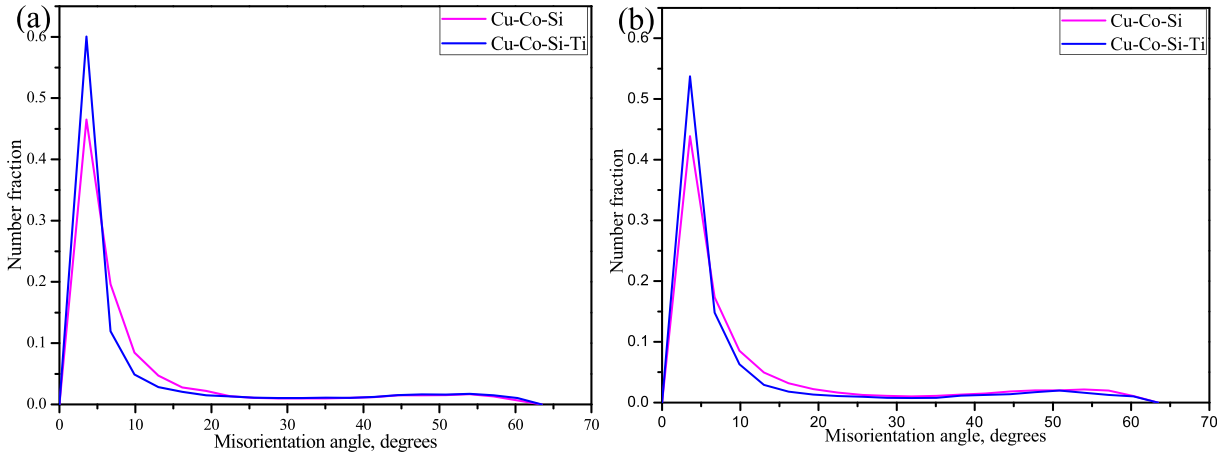

Fig. 7. Misorientation angle of Cu–Co–Si and Cu–Co–Si–Ti alloys deformed at 0.001 s^{-1} with different temperatures: (a) 700 °C; (b) 900 °C.

deformed at 700 °C and 0.001 s^{-1}. It can be determined from Fig. 11(b) that the precipitate in Fig. 11(a) is Co_2Si, which has an orthorhombic structure. The average size of Co_2Si is about 12 nm. Fig. 11(c and d) shows the bright and dark field images of the two precipitated phases, respectively. One precipitated phase is Co_2Si, and the other is petal-like precipitate. The high-resolution image and SADP of the petal-like shape precipitation phase are shown in Fig. 11(e) and (f), respectively. It is determined from Fig. 11(f) that the petal-like shape precipitation phase is Cu_4Ti, which also has orthorhombic structure and the lattice parameters are a = 4.53 nm, b = 4.342 nm, c = 12.93 nm, and $\alpha = \beta = \gamma = 90°$. The average size of Cu_4Ti is about 17 nm.

Ti plays an important role in promoting precipitation and reducing the precipitate size. Humphreys et al. [40] found that mechanical behavior, structure, and texture depend on the precipitates size. When the size of the precipitated phase is in the 0.5–2 μm range, dynamic recrystallization is more likely to occur. In other words, it can promote dynamic recrystallization. However, when the size of the precipitated phase is less than 0.5 μm, dynamic recrystallization is inhibited by pinning dislocations movement and hindering the grain boundaries migration. compared with the precipitates of Cu–Co–Si and Cu–Co–Si–Ti alloys in Figs. 10 and 11, it can be seen that the precipitation size of the Cu–Co–Si–Ti alloy is smaller and its distribution is more uniform than the Cu–Co–Si alloy. In this experiment, the precipitates in the Cu–Co–Si alloy are mainly inside the grain, and dislocations tangle near the secondary phases and grain boundaries during thermal deformation due to precipitates and grain boundaries, which hinder the movement of dislocations. Many fine precipitates dispersed in the Cu–Co–Si–Ti alloy pin dislocations and hinder the migration of grain boundaries, which increase the flow stress, activation energy for thermal deformation and inhibit dynamic recrystallization. In addition to

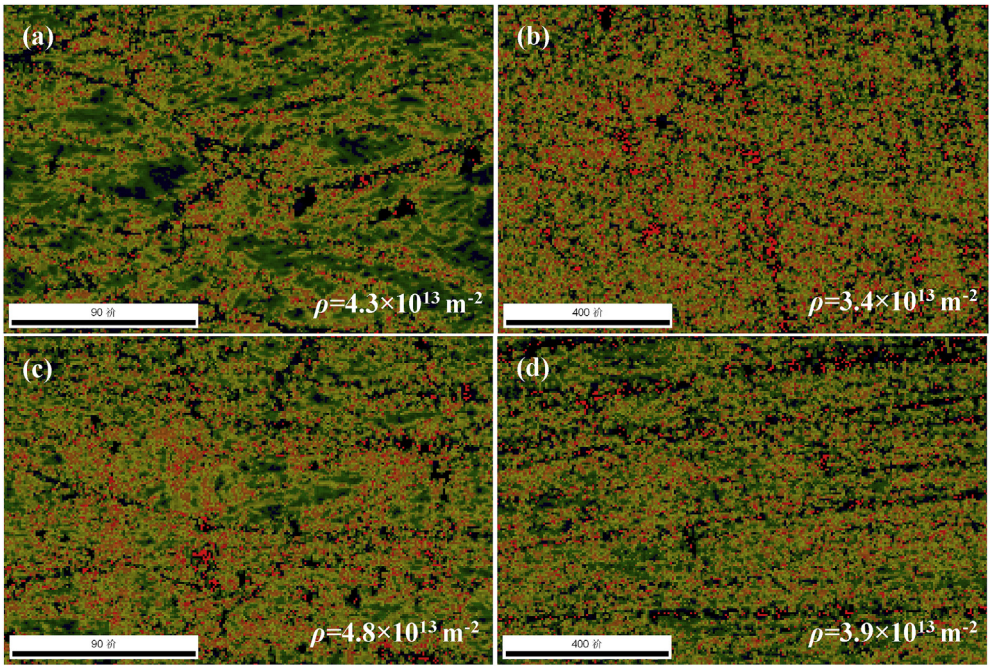

Fig. 8. The Kernel Average Misorientation (KAM) of (a)Cu–Co–Si alloy deformed 700 °C,0.001 s^{-1};(b)Cu–Co–Si alloy deformed 900 °C,0.001 s^{-1};(c)Cu–Co–Si–Ti alloy deformed 700 °C,0.001 s^{-1};(d)Cu–Co–Si–Ti alloy deformed 900 °C,0.001 s^{-1}.

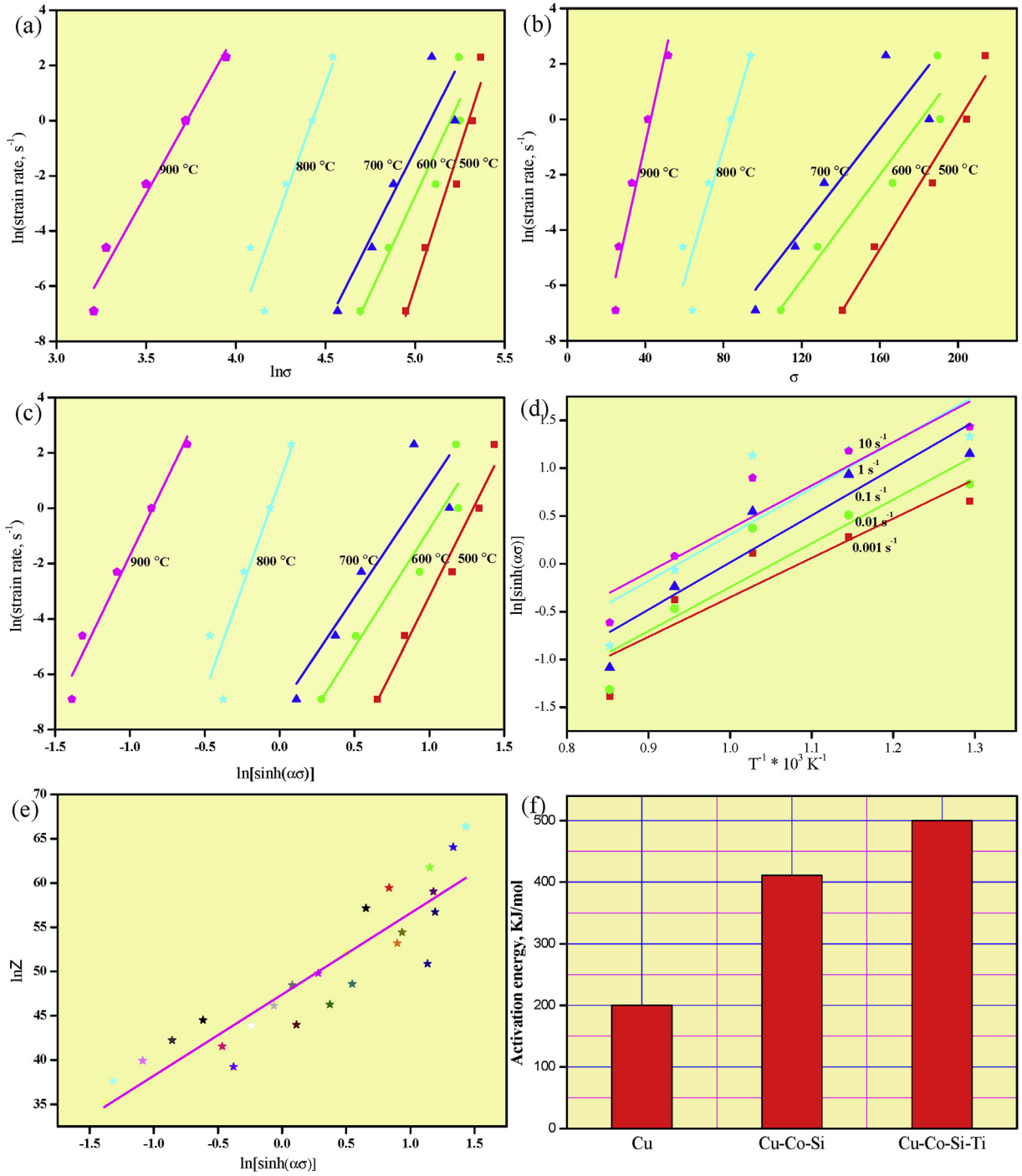

Fig. 9. Relations between: (a) ln (strain rate) and ln σ; (b) ln (strain rate) and σ; (c) ln (strain rate) and ln [sinh (ασ)]; (d) ln [sinh (ασ)] and $T^{-1} * 10^3 K^{-1}$;(e) ln Z and ln [sinh (ασ)]; (f) activation energy of the Cu, Cu–Co–Si and Cu–Co–Si–Ti alloys.

the uniform distribution of precipitated phases in the grain interior, there are several discontinuous precipitates distributed at the grain boundaries, shown in Fig. 12(a). It is determined to be Co_2Si. Finally, the precipitation phases are finer and more uniform due to the addition of Ti during hot deformation of the Cu–Co–Si and Cu–Co–Si–Ti alloys, which is defined as dispersion strengthening. In addition, many fine and uniformly distributed precipitates pin grain boundaries and dislocations due to the addition of Ti, which hinders the migration of grain boundaries and movement of dislocations, thus increasing the flow stress, activation energy and inhibiting dynamic recrystallization.

4.2. Twinning mechanism

The formation of twins is closely related to the stacking faults. According to the different reasons for the formation of twins, it can be divided into deformation, growth, and annealing twins. It is noteworthy that annealing twins can be formed in copper alloy with low stacking fault energy during dynamic recrystallization. It is well known that plastic deformation of metals is controlled by

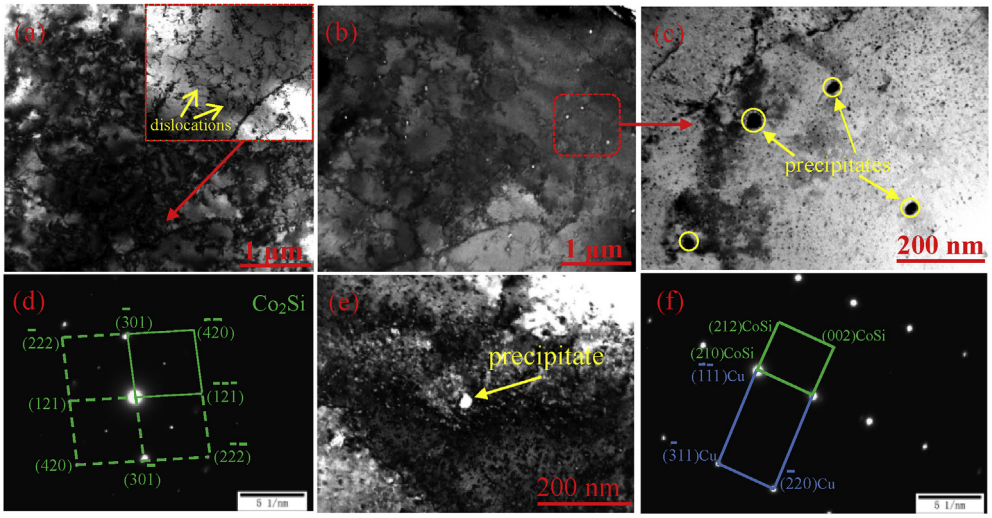

Fig. 10. The TEM graphs of Cu–Co–Si alloy deformed at 700 °C,0.001 s^{-1}:(a),(e)bright-field images; (b)dark-field image of (a); (c)magnification of red rectangle area in(b); (d)SADP of the precipitate in (c); (f)SADP of the large precipitation phase in (e). (For interpretation of the references to color in this figure legend, the reader is referred to the Web version of this article.)

both slip and twins. When dislocations are pinned by precipitated phases and grain boundaries, dislocations tangle and dislocation density increases, resulting in slip hindrance, where twins will play an important role. The formation of twins alters the orientation of crystals, which shifts the unfavorable slip system of some atoms to the position favorable to slip and stimulates further slip and crystal deformation. Fig. 12(b) shows the TEM image of the Cu–Co–Si–Ti alloy. There are several annealing twins in the structure. The existence of twin boundaries results in more grain boundaries, which can pin the movement of dislocations and hinder the migration of grain boundaries. Simultaneously, it increases the flow stress, activation energy for thermal deformation and inhibits dynamic recrystallization.

4.3. Grain refinement strengthening

There will be lots of subgrains in the matrix during hot deformation. The influence of the grain size on the yield stress can be described by the Hall-Petch equation [37]:

$$\Delta\sigma_{grain} = \frac{K}{\sqrt{d_{grain}}} \tag{12}$$

Here, k is the constant for copper alloys; d_{grain} is the average size, measured from TEM images in Fig. 12(c and d) by the Image J. The values of grain refinement strengthening are listed in Table 2.

In summary, the addition of Ti can make the precipitated phases finer and more uniform during hot deformation of the Cu–Co–Si and Cu–Co–Si–Ti alloys, which can be defined as dispersion strengthening. In addition, the movement of dislocations and migration of grain boundaries are hindered due to the existence of fine precipitated phases and annealing twins, which increases the flow stress and activation energy for thermal deformation. Higher deformation energy is required for dynamic recrystallization of the Cu–Co–Si–Ti alloy than the Cu–Co–Si alloy, which indicates that the Cu–Co–Si–Ti alloy has better high-temperature stability. The addition of Ti inhibits dynamic recrystallization of the Cu–Co–Si–Ti alloy.

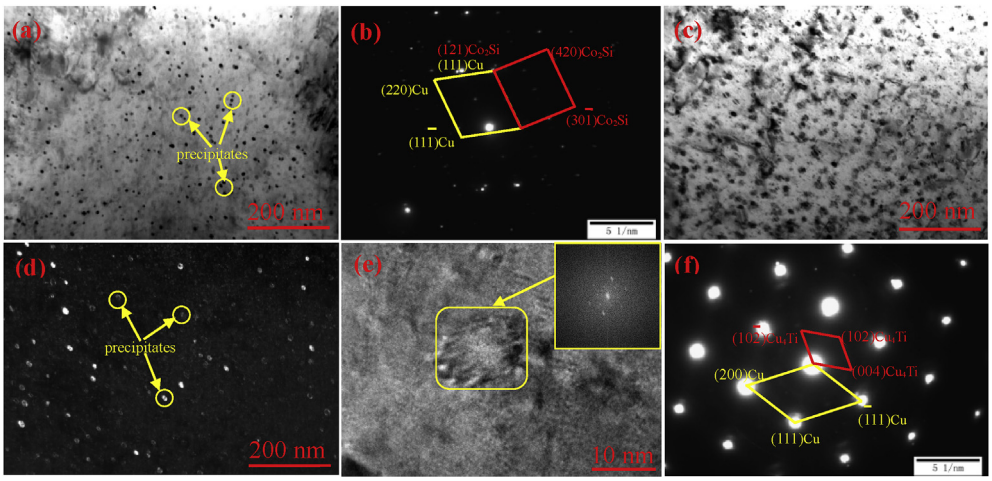

Fig. 11. The TEM graphs of Cu–Co–Si–Ti alloy deformed at 700 °C,0.001 s^{-1}:(a), (c)bright-field images; (b)SADP of the precipitate in (a); (d)dark-field image of (c); (e)high resolution image; (f)SADP of the petaloid precipitation phase in (c).

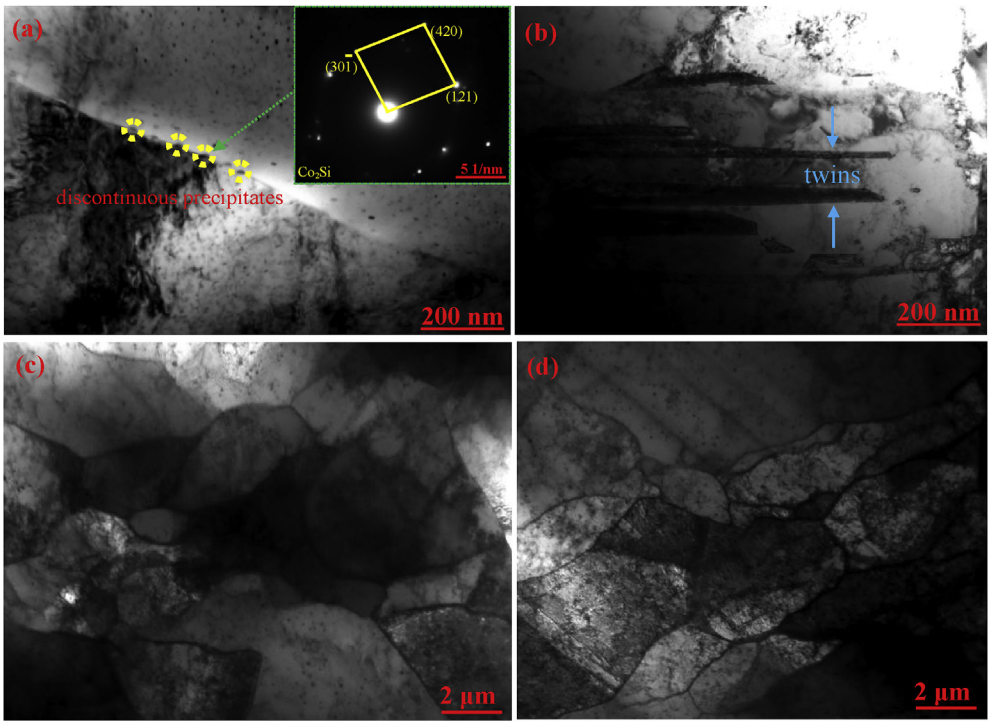

Fig. 12. TEM micrographs of: (a), (b), (d) Cu–Co–Si–Ti alloy; (c) Cu–Co–Si alloy.

Table 2
The values of the grain refinement strengthening.

parameter	Cu–Co–Si	Cu–Co–Si–Ti	units
k	0.14	0.14	$MPa \bullet m^{1/2}$
d_{grain}	0.86	0.68	um
$\Delta\sigma_{grain}$	151	170	MPa

5. Conclusions

The hot compression test of the Cu–Co–Si and Cu–Co–Si–Ti alloys were carried out using the Gleeble-1500 simulator at 0.001–10 s^{-1} strain rates and 500–900 °C deformation temperatures. The effects of Ti addition on the Cu–Co–Si alloy were discussed. Several conclusions are as follows:

(1) The flow stress increases with the decrease of temperature or the increase of strain rate. The addition of Ti increases the flow stress of the Cu–Co–Si–Ti alloy.
(2) With the deformation temperature increasing from 700 °C to 900 °C, the texture of the Cu–Co–Si alloy transformed from {112} <111> copper texture to {111} <211> R texture. However, {112} <111> copper texture and {111} <211> R texture was substituted by the {011} <100> Goss texture and {112} <111> copper texture, respectively, due to the addition of Ti.
(3) By establishing the constitutive model, the activation energy of the Cu–Co–Si alloy was 411.648 kJ/mol, and the activation energy of Cu–Co–Si–Ti alloy increased by 27% with the addition of Ti.
(4) The CoSi and Co_2Si precipitates were found in the Cu–Co–Si alloy during hot deformation, while fine and dispersed Co_2Si and Cu_4Ti precipitates were found in the Cu–Co–Si–Ti alloy.
(5) Dispersion strengthening, twinning mechanism and grain refinement strengthening control the hot deformation process of the Cu–Co–Si–Ti alloy, which increases the flow stress, activation energy for thermal deformation and inhibits dynamic recrystallization of the Cu–Co–Si–Ti alloy.

Declaration of competing interest

The authors declare that they have no known competing financial interests or personal relationships that could have appeared to influence the work reported in this paper.

Acknowledgments

This work was supported by the Open Cooperation Project of Science and Technology of the Henan Province (182106000018), Henan University Scientific and Technological Innovation Talent Support Program (18HASTIT024) and the National Natural Science Foundation of China (U1704143).

References

[1] W. Wang, H.J. Kang, Z.N. Chen, Z.J. Chen, C.L. Zou, R.G. Li, G.M. Yin, T.M. Wang, Effects of Cr and Zr additions on microstructure and properties of Cu- Ni-Si alloys, Mater. Sci. Eng. A 673 (2016) 378–390.
[2] A. Ozawa, C. Watanabe, R. Monzen, Influence of Co on strength of Cu-Ni-Co-Si alloy, Mater. Sci. Forum 783–786 (2014) 2468–2473.
[3] L. Zhang, Z. Li, Q. Lei, W.T. Qiu, H.T. Luo, Hot deformation behavior of Cu-8.0Ni-1.8Si-0.15Mg alloy, Mater. Sci. Eng. A 528 (2011) 1641–1647.
[4] Z.Q. Wang, Y.B. Zhong, G.H. Cao, C. Wang, Influence of dc electric current on the hardness of thermally aged Cu-Cr-Zr alloy, J. Alloy. Comp. 479 (2009) 303–306.
[5] R. Monzen, C. Watanabe, Microstructure and mechanical properties of Cu-Ni-Si alloys, J. Alloy. Comp. 483–484 (2008) 117–119.
[6] Y. Zhang, H.L. Sun, A.A. Volinsky, B.H. Tian, K.X. Song, B.J. Wang, Y. Liu, Hot workability and constitutive model of the Cu-Zr-Nd alloy, Vacuum 146 (2017) 35–43.
[7] H. Tsubakino, R. Nozato, A. Yamamoto, Discontinuous and continuous coarsening of lamellar precipitates in Cu-Be alloys, J. Mater. Sci. 26 (1991) 2851–2856.
[8] H.L. Sun, Y. Zhang, A.A. Volinsky, B.J. Wang, B.H. Tian, K.X. Song, Z. Chai, Y. Liu, Effects of Ag addition on hot deformation behavior of Cu-Ni-Si Alloys, A. Eng. Mater. 19 (2017) 1600607.

[9] S.F. Fang, Prediction of the hardness of Cu-Ti-Co alloy using machine learning Techniques, Key Eng. Mater. 777 (2018) 372–376.
[10] E. Lee, K. Euh, S.Z. Han, S. Lim, J. Lee, S. Kim, Tensile and electrical properties of direct aged Cu-Ni-Si-x%Ti alloys, Met. Mater. Int. 19 (2013) 183–188.
[11] C. Watanabe, R. Monzen, S. Ii, K. Tsuchiya, Microstructure and aging behavior of Cu-Be alloy processed by high-pressure torsion, Mater. Sci. Forum 783–786 (2014) 2707–2712.
[12] Q. Lei, Z. Li, Y. Gao, P. Xi, B. Derby, Microstructure and mechanical properties of a high strength Cu-Ni-Si alloy treated by combined aging processes, J. Alloy. Comp. 695 (2017) 2413–2423.
[13] Z. Zhao, Y. Zhang, B.H. Tian, Y.L. Jia, Y. Liu, K.X. Song, A.A. Volinsky, Co effects on Cu-Ni-Si alloys microstructure and physical properties, J. Alloy. Comp. 797 (2019) 1327–1337.
[14] Y.J. Zhou, K.X. Song, J.D. Xing, Y.M. Zhang, Precipitation behavior and properties of aged Cu-0.23Be-0.84Co alloy, J. Alloy. Comp. 658 (2016) 920–930.
[15] S.C. Krishna, J. Srinath, A.K. Jha, B. Pant, K.M. George, Microstructure and properties of a high-strength Cu-Ni-Si-Co-Zr alloy, J. Mater. Eng. Perform. 22 (2013) 2115–2120.
[16] H.G. Kim, T.W. Lee, S.M. Kim, S.Z. Han, K. Euh, W.Y. Kim, S.H. Lim, Effects of Ti addition and heat treatments on mechanical and electrical properties of Cu-Ni-Si alloys, Met. Mater. Int. 19 (2013) 61–65.
[17] J. Liu, X.H. Wang, T.T. Guo, J.T. Zou, X.H. Yang, Microstructural evolution and properties of aged Cu-3Ti-3Ni Alloy, R. Met. Mater. Eng. 45 (2016) 1162–1167.
[18] Z.T. Wang, R.Z. Tian, Copper Alloy and its Processing Manual, vol. 2, Central South University Press, Hunan, China, 2002, p. 11 (In Chinese).
[19] Y.X. Liu, M.X. Zhao, Z. Li, B.H. Chen, F.C. Yin, Phase equilibria of the Co-Cu-Zn system at 600 °C and 450 °C, Calphad 62 (2018) 119–127.
[20] B.J. Wang, Y. Zhang, B.H. Tian, V. Yakubov, J.C. An, A.A. Volinsky, Y. Liu, K.X. Song, L.H. Li, M. Fu, Effects of Ce and Y addition on microstructure evolution and precipitation of Cu-Mg alloy hot deformation, J. Alloy. Comp. 781 (2019) 118–130.
[21] C. Roucoules, M. Pietrzyk, P.D. Hodgson, Analysis of work hardening and recrystallization during the hot working of steel using a statistically based internal variable model, Mater. Sci. Eng. A 339 (2003) 1–9.
[22] Y.Q. Ning, X. Luo, H.Q. Liang, H.Z. Guo, J.L. Zhang, K. Tan, Competition between dynamic recovery and recrystallization during hot deformation for TC18 titanium alloy, Mater. Sci. Eng. A 635 (2015) 77–85.
[23] Z.Y. Dong, S.G. Jia, P.F. Zhao, M. Deng, K.X. Song, Hot deformation behavior of Cu-0.6Cr-0.03Zr alloy during compression at elevated temperatures, Mater. Sci. Eng. A 570 (2013) 87–91.
[24] G.L. Ji, G. Yang, L. Li, Q. Li, Modeling constitutive relationship of Cu-0.4 Mg alloy during hot deformation, J. Mater. Eng. Perform. 23 (2014) 1770–1779.
[25] G.X. Qiu, D.P. Zhan, C.S. Li, M. Qi, Z.H. Jiang, H.S. Zhang, Effects of Y and Ti addition on microstructure stability and tensile properties of reduced activation ferritic/martensitic steel, Nucl. Eng. Technol. 51 (2019) 1365–1372.
[26] X.S. Zhou, C. Li, L.M. Yu, H.J. Li, Y.C. Liu, Effects of Ti addition on microstructure and mechanical property of spark-plasma-sintered transformable 9Cr-ODS steels, Fusion Eng. Des. 135 (2018) 88–94.
[27] H. Miura, M. Watanabe, T. Shirai, A. Ishibashi, Mechanisms of dynamic recrystallization in Cu-Sn-P Alloy, Mater. Sci. Forum 654–656 (2010) 1267–1270.
[28] Q. Lei, Z. Li, W.P. Hu, Y. Liu, C.L. Meng, B. Derby, W. Zhang, Microstructure evolution and hardness of an ultra-high strength Cu-Ni-Si alloy during thermo-mechanical processing, J. Mater. Eng. Perform. 25 (2016) 2615–2625.
[29] J.J. Sidor, L.A.I. Kestens, Analytical description of rolling textures in face-centered-cubic metals, Scr. Mater. 68 (2013) 273–276.
[30] W.J. He, A. Chapuis, X. Chen, Q. Liu, Effect of loading direction on the deformation and annealing behavior of a zirconium alloy, Mater. Sci. Eng. A 734 (2018) 364–373.
[31] Y.S. Wu, X.Z. Qin, C.S. Wang, L.Z. Zhou, Influence of phosphorus on hot deformation microstructure of a Ni-Fe-Cr based alloy, Mater. Sci. Eng. A 768 (2019) 138454.
[32] C.M. Sellars, W.J. McTegart, On the mechanism of hot deformation, Acta Metall. 14 (1966) 1136–1138.
[33] H. Mirzadeh, Constitutive analysis of Mg-Al-Zn magnesium alloys during hot deformation, Mech. Mater. 77 (2014) 80–85.
[34] H. Mirzadeh, Quantification of the strengthening effect of reinforcements during hot deformation of aluminum-based composites, Mater. Des. 65 (2015) 80–82.
[35] A.K. Shukla, S.V.S. Narayana Murty, S.C. Sharma, K. Mondal, Constitutive modeling of hot deformation behavior of vacuum hot pressed Cu-8Cr-4Nb alloy, Mater. Des. 75 (2015) 57–64.
[36] B.J. Wang, Y. Zhang, B.H. Tian, J.C. An, A.A. Volinsky, H.L. Sun, Y. Liu, K.X. Song, Effects of Ce addition on the Cu-Mg-Fe alloy hot deformation behavior, Vacuum 155 (2018) 594–603.
[37] Z.L. Zhao, X. Zhu, Z. Li, W.T. Qiu, H.Y. Jiang, Q. Lei, Z.R. Liu, Y.B. Jiang, S.J. Zhang, Microstructure and properties of a Cu-Ni-Si-Co-Cr alloy with high strength and high conductivity, Mater. Sci. Eng. A 759 (2019) 396–403.
[38] X.P. Xiao, Z.Y. Yi, T.T. Chen, R.Q. Liu, H. Wang, Suppressing spinodal decomposition by adding Co into Cu-Ni-Si alloy, J. Alloy. Comp. 660 (2016) 178–183.
[39] J. Liu, X.H. Wang, J.T. Liu, Y.F. Liu, H.Y. Li, C. Wang, Hot deformation and dynamic recrystallization behavior of Cu-3Ti-3Ni-0.5Si alloy, J. Alloy. Comp. 782 (2019) 224–234.
[40] F.J. Humphreys, P.N. Kalu, Dislocation-particle interactions during high temperature deformation of two-phase aluminum alloys, Acta Metall. 35 (1987) 2815–2829.